Eliminating redox-mediated electron transfer mechanisms on a supported molecular catalyst enables CO2 conversion to ethanol

Abdinejad, Maryam; Farzi, Amirhossein; Möller-Gulland, Robin; Mulder, Fokko; Liu, Chengyu; Shao, Junming; Biemolt, Jasper; Robert, Marc; Seifitokaldani, Ali; Burdyny, Thomas

DOI
10.1038/s41929-024-01225-1

Publication date
2024

Document Version
Final published version

Published in
Nature Catalysis

Citation (APA)
Abdinejad, M., Farzi, A., Möller-Gulland, R., Mulder, F., Liu, C., Shao, J., Biemolt, J., Robert, M., Seifitokaldani, A., & Burdyny, T. (2024). Eliminating redox-mediated electron transfer mechanisms on a supported molecular catalyst enables CO2 conversion to ethanol. *Nature Catalysis*, *7*(10), 1109-1119. https://doi.org/10.1038/s41929-024-01225-1

nature catalysis

Article

https://doi.org/10.1038/s41929-024-01225-1

Eliminating redox-mediated electron transfer mechanisms on a supported molecular catalyst enables CO_2 conversion to ethanol

Received: 18 June 2023

Accepted: 14 August 2024

Published online: 13 September 2024

Check for updates

Maryam Abdinejad[1,2,7] ✉, Amirhossein Farzi[3,7], Robin Möller-Gulland[1,7], Fokko Mulder[1], Chengyu Liu[4], Junming Shao[4], Jasper Biemolt[1], Marc Robert[4,5,6], Ali Seifitokaldani[3] ✉ & Thomas Burdyny[1] ✉

Molecular catalysts play a significant role in chemical transformations, utilizing changes in redox states to facilitate reactions. To date molecular electrocatalysts have efficiently produced single-carbon products from CO_2 but have struggled to achieve a carbon–carbon coupling step. Conversely, copper catalysts can enable carbon–carbon coupling, but lead to broad C_{2+} product spectra. Here we subvert the traditional redox-mediated reaction mechanisms of organometallic compounds through a heterogeneous nickel-supported iron tetraphenylporphyrin electrocatalyst, facilitating electrochemical carbon–carbon coupling to produce ethanol. This represents a marked behavioural shift compared with carbon-supported metalloporphyrins. Extending the approach to a three-dimensional porous nickel support with adsorbed iron tetraphenylporphyrin, we attain ethanol Faradaic efficiencies of 68% ± 3.2% at −0.3 V versus a reversible hydrogen electrode (pH 7.7) with partial ethanol current densities of −21 mA cm^{-2}. Separately we demonstrate maintained ethanol production over 60 h of operation. Further consideration of the wide parameter space of molecular catalyst and metal electrodes shows promise for additional chemistries and achievable metrics.

Many organometallic molecular compounds can function as excellent catalysts for carbon dioxide (CO_2) reduction due to their ability for their reduced forms to spontaneously form an adduct[1]. Through oxidation of the molecular catalyst and electron donation, CO_2 can then be reduced to value-added products. However, the redox-mediated mechanisms of molecular catalysts mean that electrons cannot be donated ad infinitum, and the oxidation state of the molecular catalyst must be regenerated through an electrode or electron donors prior to further reductions (Fig. 1a). Although efficient, the mechanism of CO_2 reduction on molecular catalysts has traditionally been limited to two-electron products such as carbon monoxide (CO) and formate ($HCOO^-$) due at least partly to the limited oxidation states of organometallic compounds before requiring regeneration. Modifications to the molecular structure, the addition of proton–electron donors and tandem catalysis scenarios can allow for conversion to higher-electron products, but demonstrations have been scarce[2,3]. To improve electron

[1]Department of Chemical Engineering, Delft University of Technology, Delft, Netherlands. [2]Department of Chemical Engineering, Massachusetts Institute of Technology, Cambridge, MA, USA. [3]Department of Chemical Engineering, McGill University, Montreal, Quebec, Canada. [4]Université Paris Cité, CNRS, Laboratoire d'Electrochimie Moléculaire, Paris, France. [5]Sorbonne Université, CNRS, Institut Parisien de Chimie Moléculaire, Paris, France. [6]Institut Universitaire de France (IUF), Paris, France. [7]These authors contributed equally: Maryam Abdinejad, Amirhossein Farzi, Robin Möller-Gulland. ✉e-mail: maryamab@mit.edu; ali.seifitokaldani@mcgill.ca; T.E.Burdyny@tudelft.nl

https://doi.org/10.1038/s41929-024-01225-1

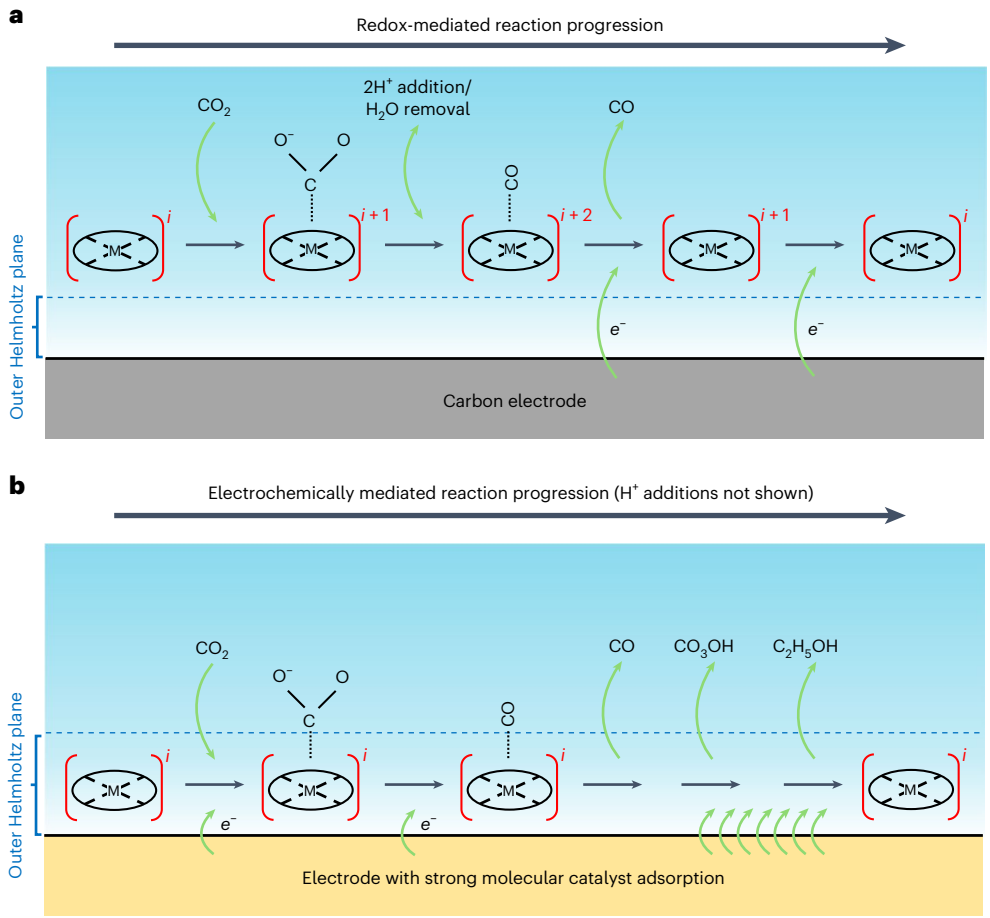

Fig. 1 | Redox- and non-redox-mediated electrochemical CO_2 reduction pathways on supported organometallic catalysts. a, Schematic representation of a general redox-mediated reaction mechanism using organometallic molecular catalysts for CO_2 reduction. Here the molecular catalyst reduces CO_2 to CO and is then regenerated via electron transfers from an inert electrode. **b**, Schematic representation of an electrochemical reaction mechanism in which a molecular catalyst resides inside the electric double layer. Here electron transfers from the electrode occur during the CO_2 reduction reaction, preventing substantial oxidation of the hybrid organometallic catalyst or its metal centre.

regeneration and the turnover number of molecular catalysts, they have been immobilized primarily onto inert carbon-based electrodes such as graphene and nanotubes. Although this has allowed for current densities >100 mA cm^{-2}, demonstrations of higher-electron products have not proliferated, indicating that additional limitations still exist.

One such limitation lies in the changes in the metal oxidation states during the redox-mediated reduction of CO_2. During reduction of the CO_2 adduct, the oxidation state of the metal centre (which is typically characterized as binding to CO_2 and its intermediates) also varies. Changes in the oxidation state upon successive electron or proton transfers then greatly modify the binding energy of the metal site to the CO_2 reduction intermediates. For example, in the classical case of iron porphyrins[4] the reduction of Fe(II) to Fe(I) facilitates the release of *CO. If the Fe(II) state were instead maintained, CO would be strongly bound to iron, similar to what happens during CO poisoning of haemoglobin. Although the oxidation state changes to Fe(I) allows for the release of CO as a product, it inhibits the reduction and coupling of CO intermediates into higher-electron products such as methane (CH_4), methanol (CH_3OH), ethylene (C_2H_4) and ethanol (C_2H_5OH).

Conversely, in bulk metals delocalized electrons allow for continuous electrons to be supplied for CO_2 reduction under an applied potential. Only copper and copper-based catalysts, however, can obtain higher-electron products at meaningful current densities due to their moderate binding energy towards CO which allows for further reductions. Thus copper catalysts have enabled ethylene and ethanol selectivity independently >50%, and collectively >85%[5–17]. Problematically, however, the branching pathway between ethylene and oxygenates on copper is downhill from the rate-determining steps, leaving few means of experimentally shifting ethylene:oxygenate ratios. Selective production of a specific multicarbon product is then highly challenging.

Despite their limitations to date, molecular catalysts have long been hypothesized to yield higher-electron products if a strong enough interaction exists between the catalyst and substrate. Under these conditions, the molecular catalyst could be positioned inside the electric double layer, which would allow for electrons to be shuttled through the catalyst at rates faster than their consumption in the CO_2 reduction reaction. The local oxidation state of the metal site could then remain fixed (schematic in Fig. 1b)[3,18]. Under such conditions, the molecular catalyst would then function as a hybrid electrocatalyst with a potential modulated by the electrode, thus breaking redox-mediated limitations. A recent example using a molecular catalyst directly conjugated to graphene has shown such behaviour. Here the oxidation state remains fixed due to the molecular catalyst residing inside the electric double layer[19], creating metal-like molecules[20]. Such behaviour was in part attributed to the lack of solvation in aqueous media of the hydrophobic cobalt tetraphenylporphyrin.

In this study, we demonstrate CO_2 electroconversion to ethanol as the primary reduction product on a combined nickel electrode and iron tetraphenylporphyrin (Fe-TPP) catalyst. The single C_2 production of ethanol stands in contrast to copper-based systems that produce a mixture of C_2 products such as ethanol, acetate and ethylene.

Through computational analysis and a series of control experiments we hypothesize that strong coupling of Fe-TPP to nickel facilitates rapid electron shuttling and stabilizes the metal oxidation state, allowing for higher-electron transfers to occur. We then extend these results to a larger three-dimensional (3D) nickel structure, reaching 68% ethanol selectivity at low potentials. The results are supported by in situ and ex situ X-ray absorption near-edge spectroscopy (XANES)/X-ray absorption spectroscopy (XAS) studies and by density functional theory (DFT) calculations, which discuss the ethanol formation mechanism and the absence of other higher-electron products.

Results

Coupling a Fe-TPP molecular catalyst to a nickel electrode

To circumvent the traditional limitations of molecular catalysts, we sought to create strong electronic coupling between a catalyst and an electrode support. Although carbon-based materials have traditionally been used as a catalyst support due to their relatively inert electrochemical behaviour, several characterization and electrochemical studies have reported that strong chemisorption-type interactions[21–27] are possible using metal supports. Furthermore, X-ray photoelectron spectroscopy examining cobalt(II) phthalocyanine adsorbed onto Ag(111), and Ni(111) has also seen direct electronic interactions between the metal centre and electrode, resulting in electron density transfer from cobalt to the more electronegative silver and nickel metals[23,26,27]. We then hypothesized that during electrochemical applications, such interactions could then stabilize oxidation states while facilitating continuous electron transfers. In addition, the binding energies of *CO to an organometallic metal centre could be modulated by the choice of metal electrode.

With these principles in mind, we aimed to combine a metal electrode with a molecular catalyst. Fe-TPP is a logical molecular catalyst to test due to its efficient production of CO and its well-understood oxidation states during CO_2 reduction[28]. Nickel was chosen as a metal support due to its relative inertness for CO_2 reduction[29,30] and its previously reported interactions with molecular catalysts. We then performed DFT computations to compare the adsorption of Fe-TPP on graphene versus Ni(111) (see Supplementary Information for computational details). Our DFT computations showed the iron site was within 2.00 Å of the nickel surface, with a shift in electron density from the iron site to the nickel atoms (Fig. 2a). Such interactions between nickel and iron have previously been shown to decrease the orbital energy levels, which increased the oxidation state of iron but with reduced binding energies for *CO (ref. 31). The comparable graphene case, however, is more reminiscent of weak physisorption with 3.92 Å between the carbon and the iron site and an intact electronic structure of the carbon atoms (Fig. 2b).

Following these results, we then drop-cast Fe-TPP onto a nickel mesh and applied cathodic potentials under both CO_2- and CO-saturated electrolytes in a flow cell (Fig. 2c and Supplementary Fig. 1) and an H-cell, respectively. For the CO_2-saturated electrolyte, ethanol was observed to be the dominant reaction product at a Faradaic efficiency (FE) of 58.2% after 4 h of operation with an applied potential of −0.3 V versus a reversible hydrogen electrode (RHE), with ethanol steadily increasing during the initial hours of operation (Fig. 2d). The ethanol partial current density at the end of the experiment was 0.37 mA cm^{-2}. The remaining products were CO and H_2. The lower initial ethanol FE may indicate that *CO or *CHO must accumulate sufficiently before coupling can occur. Such a result is notably distinct from previous studies over many years in which Fe-TPP has been reported to produce only CO and H_2.

Additionally, a 47% FE towards ethanol, with j(ethanol) = −0.23 mA cm^{-2}, was observed when CO was directly used as a reactant (Fig. 2e), with an additional 57% FE for H_2 (Supplementary Fig. 2). The CO reduction experiment indicates that the iron oxidation state in the complex can bind directly to CO, and thus may not be the Fe(I) traditionally hypothesized. The analysis of the liquid phase upon ^{1}H NMR revealed the formation of ethanol as only liquid product, as shown by the presence of a triplet peak at 1.17 ppm and a quartet peak at 3.64 ppm (Fig. 2f).

For the 12 electron transfers needed to form ethanol, and for *CO not to desorb from Fe-TPP, it is anticipated that the oxidation state of the iron site centre remains fixed throughout all the CO_2 reduction steps and is more oxidized than Fe(I). To examine the oxidation state of iron during the process, we performed in situ and ex situ XANES on Fe-TPP drop-cast on to sputtered nickel (Fe-TPP/Ni) (Supplementary Fig. 3). Applied potentials from −0.1 V to −3.0 V versus RHE were examined (Supplementary Fig. 4 and Supplementary Table 1). A systematic comparison of normalized XAS spectra of various Fe-TPP loadings on nickel was carried out (Fig. 2g). Fe(II), Fe(III) and iron foil as Fe(0) were used as references. In the case of Fe-TPP powder, iron appears in the Fe(II) and Fe(III) oxidation states, but when depositing it on nickel catalysts, Fe(0) and Fe(III) become the main oxidation states.

Figure 2g and Supplementary Table 2 show the impact of varying the Fe-TPP loading on nickel on the oxidation state of the iron centre. As the sample loading increases, a greater presence of the Fe(III) oxidation state was detected. The similarity of the lowest-energy transitions, due to weak $1s \rightarrow 3d$ pre-edge peaks at approximately 7,111–7,113 eV, indicate a similar electronic structure of the iron centre in all cases[32,33]. The Fe center of Fe-TPP clearly shows the highest-energy pre-edge feature, similar to ferric iron (Fe(III), whereas depositing Fe-TPP on nickel shows lower-energy pre-edges at ~7,111 eV. These observations suggest that the oxidation state of Fe-TPP is similar to the ferric iron (Fe(III)). However, the line shape changes with higher loadings, which can be due to a change of the oxidation state of iron from Fe(III) to Fe(0) (ref. 34). The correlation of this second peak with nickel is further substantiated by the observed trend illustrated in Supplementary Fig. 5. In this context, the emergence and intensification of the metal–metal interaction are evident as the system progresses toward the formation of the Fe-TPP monolayer on nickel.

Development of a 3D nickel-supported Fe-TPP electrocatalyst

To obtain higher selectivity and current density, we sought to increase the surface loading of Fe-TPP on nickel to increase CO_2 reduction and reduce by-product hydrogen production, which probably comes from the nickel substrate. For this reason, we designed and fabricated a 3D, highly porous nickel electrode (Fig. 3a,b and Supplementary Figs. 7–11). After deposition of Fe-TPP by drop-casting with dichloromethane, an Fe-TPP/Ni electrode was formed (Fig. 3c,d and Supplementary Figs. 13 and 14). The corresponding elemental mapping using energy-dispersive X-ray spectroscopy (EDX) shows a uniform distribution of iron, nickel, nitrogen and carbon on the collected sample from the electrode surface after deposition, which confirms that Fe-TPP is distributed on the nickel surface (Supplementary Figs. 15 and 16). Next, X-ray photoelectron spectroscopy (XPS), shown in Supplementary Figs. 17–19, was used to investigate the bonding and surface electronic states for both bare nickel and the Fe-TPP/Ni catalysts. The fabricated electrodes were positioned in a custom-designed flow cell for electrochemical testing during which CO_2 flows through the pores of the electrode (Fig. 3e, Supplementary Figs. 20–24). Here the hydrophobic Fe-TPP catalyst was deposited without a binding agent and remains fixed in the micropores of the sintered nickel electrode even during electrolyte immersion and during electrochemical operation.

The electrocatalytic activity of the designed system for CO_2RR was examined by cyclic voltammetry (Supplementary Fig. 25) and chronoamperometry with and without electrolyte flow in aqueous solutions of 0.5 M $KHCO_3$ (Supplementary Figs. 26 and 27). No strong correlation was found between $KHCO_3$ concentration and ethanol production (Supplementary Fig. 28). We chose 0.5 M concentrations for the remainder of the tests, with CO_2 was purging through the bottom of the reactor (pH 7.7). The results presented here focus on the

https://doi.org/10.1038/s41929-024-01225-1

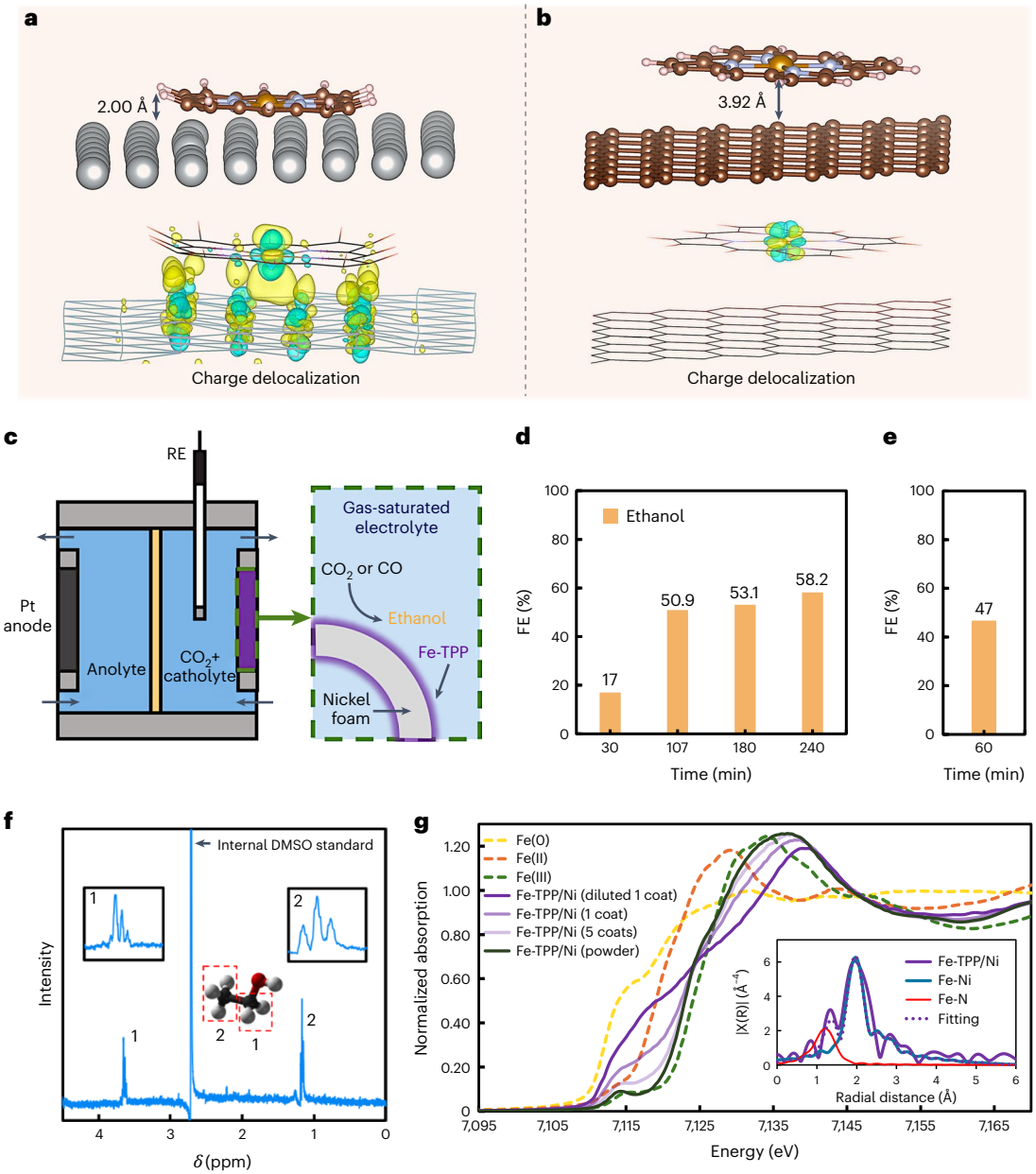

Fig. 2 | Computed interactions of a combined Fe-TPP/Ni catalyst and electrochemical characterization. a,**b**, Upper: atomic positions of Fe-TPP on nickel (**a**) and graphene (**b**); the minimum distance between the substrate and the iron centre is indicated. Lower: charge delocalization graphs of immobilized Fe-TPP on nickel (**a**) and graphene (**b**), both at an isosurface level of 0.008 e bohr^{-3} calculated with DFT. Yellow shows the electrons accepted, and blue shows the charge donated. **c**, Schematic of the CO_2 flow cell used in the experiments, and the combined Fe-TPP/Ni catalyst. **d**, Ethanol production after 4 h electrolysis of Fe-TPP/Ni foam under CO_2 at −0.30 V versus RHE in a flow cell. **e**, Ethanol production after 4 h of electrolysis of Fe-TPP/Ni in an H-cell under CO at −0.30 V versus RHE in an H-cell. **f**, ^{1}H NMR spectrum of the electrolyte after electrolysis (E = −0.30 V versus RHE, t = 4 h) in CO_2-saturated solution. The red dashed boxes highlight the locations of protons 1 and 2 in the NMR spectrum. **g**, In situ XANES of Fe-TPP/Ni catalyst with various deposition coating catalysts.

flow system shown in Fig. 3e. Three additional control catalysts were also created and tested to elucidate the effect of coupling Fe-TPP to the nickel electrode. These include a bare 3D nickel structure, TPP deposited onto nickel without an iron metal site, and a comparable 3D carbon structure covered with Fe-TPP (named Fe-TPP/C; Supplementary Fig. 29). Comparing the cyclic voltammetry curves of these catalysts (Fig. 3f) shows a large deviation in current versus voltage, with the Fe-TPP/Ni showing substantially higher current densities in the range of −0.3 to −0.6 V versus RHE.

The FEs of the four different catalysts were then examined via chronoamperometry over a range of potentials. Different CO_2 gas flow rates between 10 and 50 standard cubic centimetres per minute (sccm) were examined (Supplementary Fig. 30), and 40 sccm was selected as an optimal flow rate. The 40 sccm chronoamperometry results are shown in Fig. 3g,h and Supplementary Figs. 31 and 32 for Fe-TPP/Ni. Here Fe-TPP/C and the bare nickel samples showed only CO and H_2 as products as expected from literature, with nickel showing <20% FE for CO. Conversely, the Fe-TPP/Ni catalyst produced ethanol as a product with a 68% ± 3.2% FE at −0.3 V versus RHE and a current density of −31 mA cm^{-2}. Traces of methanol, propanol and a 3% selectivity for CO were also observed (Supplementary Figs. 33–36 and Supplementary Table 4). The only C_2 product detected is then ethanol, in contrast to copper electrodes which produce substantial hydrocarbon and oxygenate side products such as ethylene and acetate. Notably, the formation

https://doi.org/10.1038/s41929-024-01225-1

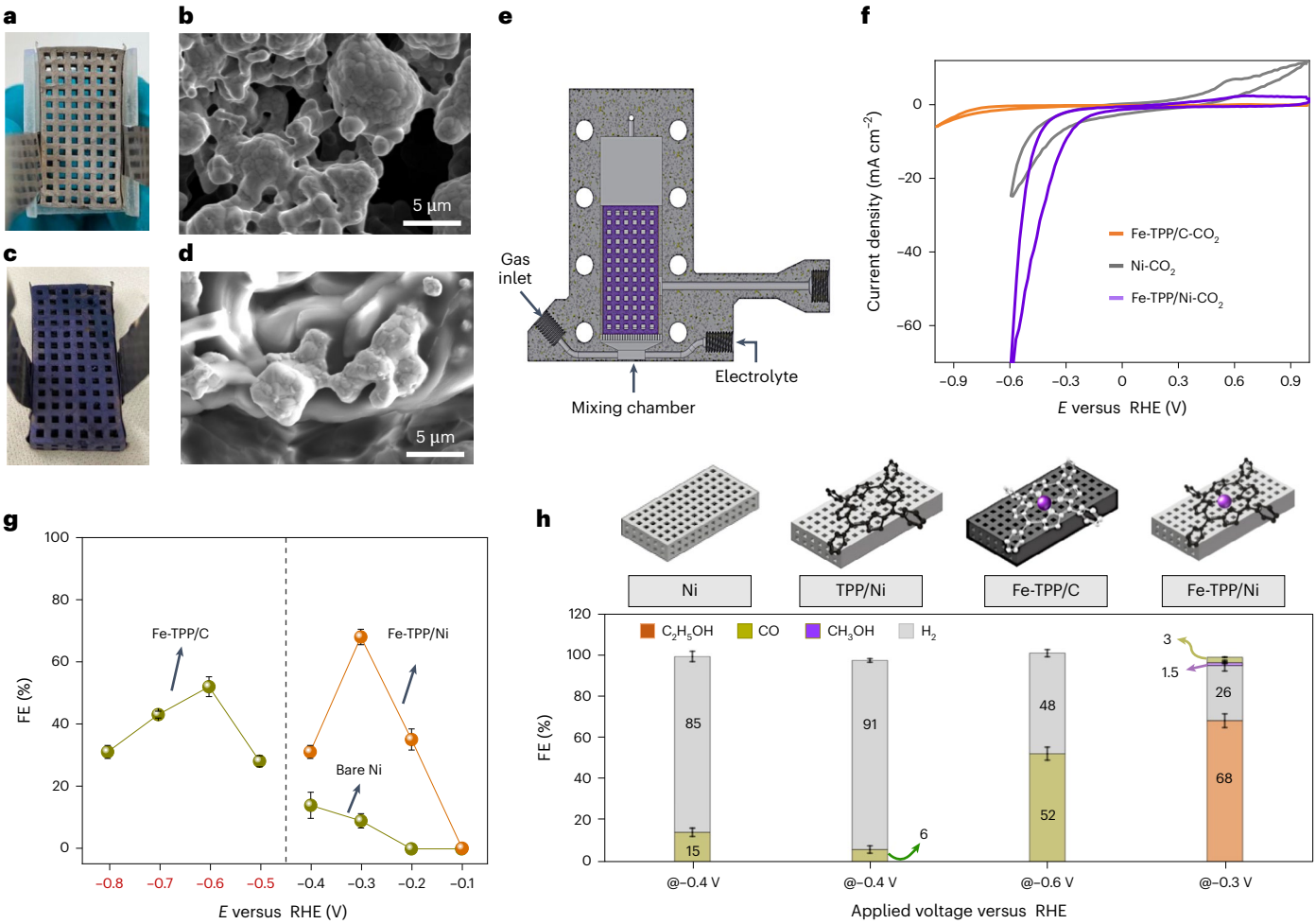

Fig. 3 | Characterization and performance of Fe-TPP/Ni and Fe-TPP/C electrodes in CO_2 electroreduction. a,**b**, Macroscopic (**a**) and SEM (**b**) images of a 3D porous nickel electrode. **c**,**d**, Macroscopic (**c**) and SEM (**d**) images of a 3D porous nickel electrode with Fe-TPP drop-cast on top using DCM (Fe-TPP/Ni). **e**, Schematic of a cell design for electrochemical testing of the 3D electrodes. **f**, Cyclic voltammetry comparison of bare nickel, Fe-TPP/Ni and Fe-TPP/C under CO_2-saturated 0.5 M $KHCO_3$ aqueous electrolyte. **g**, Comparison of the FE of the major products of Fe-TPP/C, Fe-TPP/Ni and bare nickel at several potentials in 0.5 M $KHCO_3$. **h**, FE of TPP and Fe-TPP/Ni at their optimal potential of −0.3 V; bare nickel at the optimal potential of −0.4 V; and Fe-TPP/C at the optimal potential of −0.6 V versus RHE. The error bars in **g**,**h** represent the s.d. of four independent technical measurements. *i*, oxidation state; M, metal centre.

of three-carbon species in the form of propanol is observed, indicating higher alcohol formation can also occur. Only hydrogen evolution was observed when replacing CO_2 bubbling with N_2.

The results in Fig. 3 show that the hybrid metal electrode and molecular catalyst system can greatly modify the traditional behaviour of Fe-TPP. The absence of substantial CO as a product can be explained by the iron oxidation state remaining between Fe(II) and Fe(III) as observed in the XANES spectra in Fig. 2f, preventing the CO release typically observed upon reduction of iron to Fe(I). Further, the dominant formation of ethanol (12 electrons) as a product indicates that further CO reduction and coupling of CO intermediates is occurring in the hybrid system at substantial rates. Although inorganic nickel-oxygenate-derived electrocatalysts have demonstrated the ability to reduce CO_2 to C_2^+ products[30], nickel itself is incapable of CO_2 or CO reduction to multicarbon products at substantial reaction rates, and a pure tandem catalytic reaction between Fe-TPP and the nickel electrode cannot explain ethanol formation. A short discussion on the function of nickel itself is also warranted given recent demonstrations of short- and long-chain alkane and alkene production during CO_2 reduction[35]. Although in our Fe-TPP/Ni case we observe alcohol production at lower potentials and different rates than the alkene/alkane production of pure nickel, the various roles of nickel in electrocatalysis requires further investigation. For example, nickel binds CO strongly, meaning that the exposed nickel sites could provide a carbon–carbon coupling species. Alternatively, the poisoning or coking of nickel sites via *CO could serve the role of preventing excess H_2 formation in our case, thus allowing for higher ethanol FEs to be reached. These possibilities point to the complex role that the choice of substrate could play in modifying adsorbed molecular species, shuttling intermediates or providing competing reactions. We then hypothesize that the iron site of the molecular catalyst is able to perform further reductions of bound CO intermediates due to the strong interactions with the nickel electrode as illustrated in Fig. 1b. In essence, the hybrid catalyst appears to prevent CO release by inhibiting Fe(I) formation (Fig. 2f), while the Ni–Fe interactions could weaken the binding of *CO when iron is in Fe(II)/Fe(III) states[31].

DFT analysis

Although the above results indicate how a molecular catalyst can break redox limitations to reach higher-electron products, they do not explain how carbon–carbon coupling, which typically requires two metal atoms and CO intermediates, occurs. Notably, we have shown experimentally that ethanol can be observed as a product when using both CO_2 and CO as a reactant (Fig. 2d,e).

https://doi.org/10.1038/s41929-024-01225-1

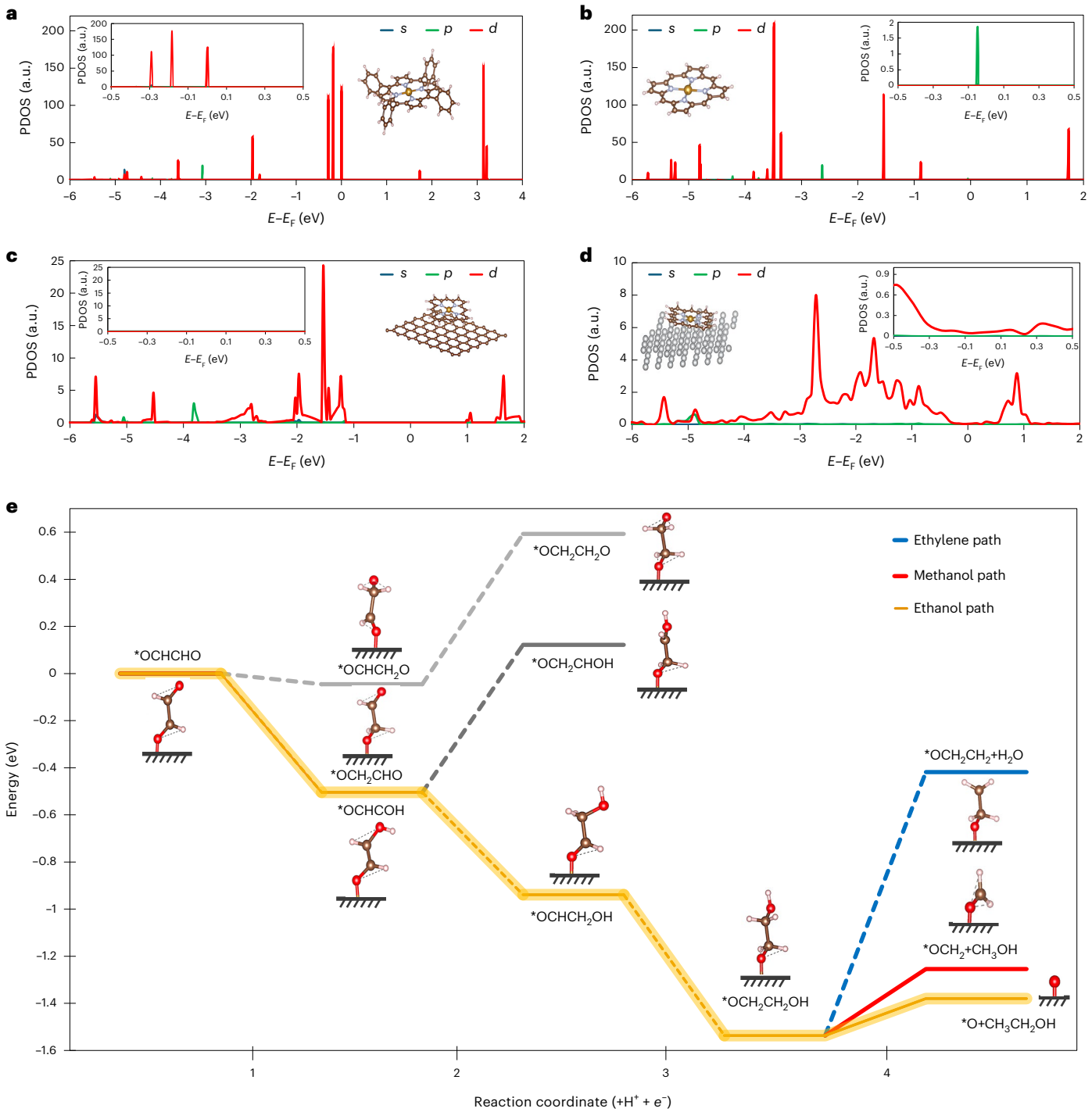

Fig. 4 | Computational calculations comparing Fe-TPP/Ni and Fe-TPP/C. **a**–**d**, Projected density of states of the iron atom in molecular Fe-TPP (**a**), modified Fe-TPP (**b**), modified Fe-TPP/C (**c**) and modified Fe-TPP/Ni (**d**). **e**, Energy diagram of possible reaction intermediates in the production of ethanol, ethylene and methanol (structures have been simplified, that is, the dashed black atom represents the Fe-TPP/Ni).

Additionally, the absence of substantial by-product CO formation on the Fe-TPP/Ni samples during CO_2 reduction indicates that tandem reactions are not dominant. Carbon–carbon coupling then appears to occur through bound intermediates. Although we cannot discern how the coupling step occurs, here we provide speculation based upon the observed experimental data and DFT. Such speculations also allow us to assess reaction mechanisms that allow alcohol to be formed on Fe-TPP/Ni without by-product ethylene (C_2H_4). The mechanism here then likely differs from that of copper electrodes where ethylene:ethanol production rates are close to 2 (ref. 36).

Fe-TPP has been extensively studied—both experimentally and computationally—as a homogeneous catalyst for the CO_2RR to two-electron products such as CO and $HCOO^-$. Thus, almost all computational studies on these types of homogeneous catalysts are limited to two proton-coupled-electron transfer steps in accordance with experimental observations. Using DFT we have extended the computational studies on Fe-TPP to further investigate the reaction energetics and mechanism beyond two proton-coupled-electron transfer steps, hypothesizing that there will be a continuous source of electrons to the iron site to activate it as soon as it is oxidized. We then aim to

https://doi.org/10.1038/s41929-024-01225-1

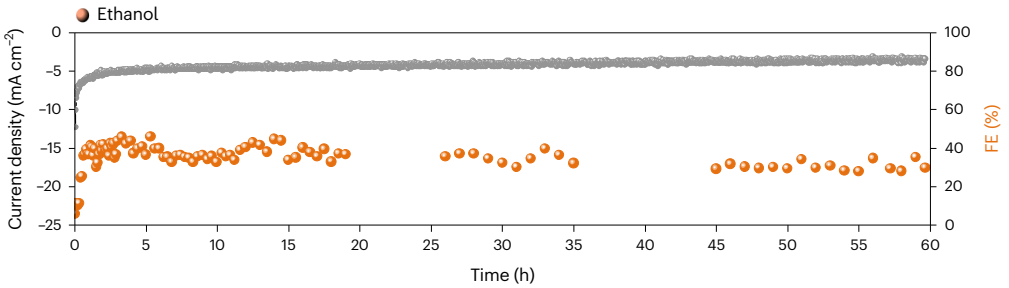

Fig. 5 | Long-term stability of a 3D Fe-TPP/Ni. Long-term stability test of Fe-TPP/Ni at a constant potential of −0.3 V versus RHE in 0.5 M $KHCO_3$ with 10 sccm CO_2.

offer insights into the electronic structure of Fe-TPP, especially when immobilized on a nickel surface, tackle the most probable pathways for the further protonation of monocarbonic intermediates, and analyse the most likely post carbon–carbon coupling reaction pathway to understand why ethanol is observed, but not alkanes/alkenes. Without experimental details supporting the coupling step, we do not provide an explicit model for the carbon–carbon coupling itself.

We then first provide a more in-depth DFT examination of the electronic impact of anchoring Fe-TPP on various substrates. We generated the densities of states for the iron core in Fe-TPP (Fig. 4a), modified Fe-TPP (Fig. 4b), where the phenyl moiety was substituted with a hydrogen atom, modified Fe-TPP/Gr (Fig. 4c), and modified Fe-TPP/Ni (Fig. 4d). Analysis of the projected densities of states, specifically considering molecular systems, revealed intermittent electron presence at various energy levels. The deposition of this structure onto a carbon substrate exhibited a broadened density of states, although non-continuous, consistent with previous findings in the literature. Conversely, when the same molecule was adsorbed onto a nickel substrate, the influence of the substrate effect was evident. In this case, a continuous and non-zero density of states was observed, extending even to the Fermi level. This outcome signifies a facilitated electron transfer from the valence band to the conduction band.

Building on the aforementioned observations, we used the modified Fe-TPP/Ni in our reaction energy calculations. This comprehensive system encompassed all important monocarbon reaction intermediates. Notably, we identified the highest reaction energy at the stage at which CO undergoes protonation. Contrary to the energetics associated with *COH formation or CO desorption (1.22 eV), we found that the thermodynamics favour the formation of *CHO (0.543 eV), as depicted in Supplementary Fig. 37. For reaction pathways in which the carbon atom is bound to iron, these simulations then indicate why CO is not observed as a major reduction product. Contrary to the Fe-TPP molecule, we found that monocarbonic species cannot adsorb onto the modified Fe-TPP/Ni through oxygen; instead, the adsorption occurs solely through the carbon atom. With the inclusion of bicarbonic intermediates, the scenario is entirely reversed, with adsorption observed solely through oxygen to the surface in both systems. Although we have not yet directly observed the mechanism of carbon–carbon coupling, given this interaction and reaction energetics of monocarbon species, we can speculate that a carbon–carbon coupling mechanism could lead to the formation of an oxygen-bound *OCHCHO intermediate.

In our final DFT analysis, we then examine further reduction pathways towards methanol, ethanol and ethylene, beginning from *OCHCHO. In particular, we observed a thermodynamic preference for the formation of the pivotal intermediate *OCH_2CH_2OH (Fig. 4e). This intermediate holds significance as it gives rise to three distinct products, depending on three different protonation scenarios. Notably, the most energy-demanding reaction occurs when protonating the OH functional group, resulting in the formation of a water molecule and *OCH_2CH_2. This intermediate is recognized for its contribution to ethylene formation. In alternative scenarios, protonation of the two carbon atoms in the key intermediate produces ethanol and methanol, with ethanol displaying higher thermodynamic favourability, as shown in Fig. 4e. The reduced reaction energies observed in the production of both ethanol and methanol, compared with the previously provided CO protonation energy, indicate the availability of the necessary energy within the reaction environment. Notably, the lower reaction energy for ethanol formation, as compared with methanol (0.157 eV versus 0.282 eV), underscores a higher FE in favour of ethanol production. Furthermore, our analysis, illustrated in Supplementary Fig. 38, indicates that the site regeneration process is characterized by consistently negative reaction energies, mitigating the risk of reaction site poisoning.

Stability test of Fe-TPP/Ni

Finally, to test the stability of the designed system over longer operating times, we operated the Fe-TPP/Ni for an initial 62 h at a constant potential of −0.3 V versus RHE under a flow rate of 10 sccm CO_2 (Fig. 5 and Supplementary Figs. 39 and 40). During the long-term reaction, a 7% decrease in ethanol selectivity was observed during the test. Furthermore, by comparing the initial and final catalyst loading, we observed a 5% decrease in the amount of Fe-TPP immobilized on the nickel. Nevertheless, no structural damage was detected following electrolysis using scanning electron microscopy (SEM) and XPS (Supplementary Figs. 42–47).

Conclusions

Here we have shown that the traditional behaviour of a molecular catalyst can be significantly altered by positioning it on a metal electrode, demonstrating both CO_2 to ethanol and CO to ethanol conversion with close to unity carbon yields. Critically we have examined only a single commonly utilized metalloporphyrin and metal electrode combination. The future variations possible to further alter electrochemical reactions and selectivity are extensive, particularly in view of the substantial existing set of molecular catalysts widely available.

Methods

Reagents and chemicals

All reagents and solvents were of commercial reagent grade and were used without further purification, except where noted. Deuterium oxide (D_2O, >99.8% D), iron(II) chloride ($FeCl_2$), *N*,*N*-diisopropylethylamine (>99%), 3-nitrobenzoic acid (99%) and potassium bicarbonate (99.7%) were purchased from Sigma-Aldrich. Nickel powder (−325 mesh, <53 µm, 99.8%) and carboxymethylcellulose sodium salt were purchased from Alfa Aesar. Nickel foam (99.5%) was purchased from Goodfellow. Araldite two-component epoxy adhesive was purchased from RS Components. H_2/Ar mixture (5%:95%) was acquired from Linde. The resins used with the Formlabs Form-2 stereolithographic 3D printer (clear and castable wax resin) were purchased from MakerPoint. Column chromatography was carried out using Caledon Silica Gel 60. Ultrapure water was generated with a Merck Milli-Q Plus 185. The CO gas used for the blank measurements is supplied by the Linde group and has the 2.0 classification, which corresponds to a purity of ≥99.0 vol.%,

with ≤4,000 ppm N_2, ≤10 ppm H_2, ≤30 ppm O_2 + Ar, ≤10 ppm C_xH_y and ≤5 ppm H_2O. The argon gas used for purging the cell before the experiments is also supplied by Linde and has the 5.0 classification, which corresponds to a purity of ≥99.999 vol.%, with <5 ppm H_2O, <5 ppm O_2 and < 0.2 ppm C_xH_y.

X-ray diffraction, XPS and SEM

The X-ray diffraction, XPS and SEM data were obtained using the Delft University of Technology research facilities. XPS measurements were performed with a Thermo Scientific K-alpha spectrometer using a monochromatic Al Kα excitation source. The spectrometer was calibrated using C 1*s* adventitious carbon with a binding energy of 284.8 eV. The base pressure at the analysis chamber was about 2×10^{-9} mbar. The spectra were recorded using a spot size of 400 µm at a pass energy of 50 eV and a step size of 0.1 eV. SEM measurements were performed on a JEOL JSM-6010LV. X-ray diffraction was performed using a Bruker D8 Advanced diffractometer with a Cu Kα source (Cu radiation wavelength: Kα1(100) = 1.54060 Å, Kα2(50) = 1.54439 Å) and a Lynxeye-XE-T position-sensitive detector. The entire Fe-TPP/Ni electrode was fixed to the sample stage. Because small inhomogeneities in the sample height exist for a large electrode, there were some shifts of the observed peak positions. This shift is corrected by comparing the measured nickel metal peaks with those from pure nickel as found in Bruker's database. With fixed-sample-illumination of 3 mm, a step size of 0.01, a measuring time of 0.02 s per step for the electrode of 2θ 5°–90°, 0.6 s per step for electrode of 2θ 5°–41° and 0.05 s per step for Fe-TPP powder of 2θ 5°–90° were used. The data were evaluated by Bruker software DiffracSuite[37,38].

XANES and extended X-ray absorption fine structure

The measurements were conducted at the Canadian Light Source (CLS) using a seven-element silicon drift detector array manufactured by Mirion Technologies. Energy steps with respect to the Fe K-edge were set at 2.0 eV intervals from −80 eV to −6 eV, and at 0.35 eV intervals from −6 eV to 40 eV. Each sample underwent two scans, and the average absorptions at each energy level were reported. A dwell time of 1 s was used for each energy level within both mentioned ranges. During the in situ tests, the gas diffusion layer was exposed to a CO_2-saturated chamber, and 0.5 M $KHCO_3$ was circulated in the anode and cathode chambers by two separate peristaltic pumps. In situ scans were conducted once per applied potential.

In situ Fe K-edge X-ray absorption spectra for Fe-TPP/Ni were obtained using the SXRMB beamline at the CLS. To simulate reaction conditions, Fe-TPP was drop-cast on 200 nm of nickel sputtered on carbon paper with a gas diffusion layer on its back. Then, using a three-compartment flow cell with CO_2 flowing in the gas chamber and 0.5 M $KHCO_3$ as the electrolyte, different constant voltages were applied to obtain the XANES plots. Before any in situ scan, we also used a vacuum chamber at 5×10^{-6} torr to obtain the ex situ extended X-ray absorption fine structure result of the same drop-cast Fe-TPP/Ni, presented in Supplementary Table 2.

The experimental procedure involved the dissolution of Fe-TPP powder in dichloromethane (DCM) at a ratio of 20 mg per 1 ml of DCM. Subsequently, samples with one, three and five coats were prepared through the spray coating method on a 100-nm-thick Ni/CP substrate, resulting in loadings of 0.5, 1.5 and 2.5 mg cm^{-2}, respectively. The process was repeated with the precursor diluted 10 and 20 times to achieve loadings of 0.05 and 0.025 mg cm^{-2}, respectively. Fe_2O_3 powder (99.995% purity) served as the Fe(III) standard, while FeO powder (99.6% purity) was used as the Fe(II) reference, both purchased from Sigma-Aldrich. The measurements were conducted at the CLS using a seven-element silicon drift detector array manufactured by Mirion Technologies. Energy steps with respect to the Fe K-edge were set at 2.0 eV intervals from −80 eV to −6 eV, and at 0.35 eV intervals from −6 eV to 40 eV. Each sample underwent two scans, and the average absorptions at each energy level were reported. A dwell time of 1 s was used for each energy level within both mentioned ranges. During the in situ tests, the gas diffusion layer was exposed to a CO_2 saturated chamber, and 0.5 M $KHCO_3$ was circulated in the anode and cathode chambers with two separate peristaltic pumps. In situ scans were conducted once per applied potential.

CO_2RR and CORR experiments

The CO_2RR and CORR experiments in Fig. 2d,e were performed at Université Paris Cité. CO_2 electrolysis was done in a flow cell, while CO electrolysis was done in an H-cell.

Preparation of deposited porphyrins on nickel foam

The nickel foam was cleaned with acetone using ultrasound for 5 min to remove organic impurities from the surface, followed by immersion in a 1 M HCl solution to remove surface oxides. A solution of Fe-TPP (32.5 mg) was made in DCM (1 ml) and was drop-cast onto the preprepared nickel foam (1 cm^2) electrode to completely cover the surface (catalyst areal loading, ~6.5 mg cm^{-2}). The electrode was dried in a vacuum oven at 50 °C for 2 h.

CO_2RR electrolysis in a flow cell

A solution of Fe-TPP (32.5 mg) was made in DCM (1 ml) and was drop-cast onto the preprepared nickel foam (1 cm^2) electrode to cover the surface completely. The electrode was dried in a vacuum oven for 2 h. Fe-TPP/Ni foam was assembled onto the cathode in the flow cell device with Ag/AgCl as a reference electrode and Pt/Ti alloy as the anode. The cathode and anode chambers were separated by a Sustainion membrane (Dioxide Materials). CO_2 gas flow was delivered at a flow rate of 20 sccm on the cathode side, while a 0.5 M $NaHCO_3$ (Sigma-Aldrich, >99.7%) electrolyte was circulated at a flow rate of 10 ml min^{-1} in both the cathode and anode chambers. The applied potential conversion from standard calomel electrode (SCE) reference to RHE reference followed the equation: E (V versus RHE) = E (V versus Ag/AgCl) + 0.197 + 0.059pH. The electrolysis experiment was conducted using a PARSTAT 4000A potentiostat (Princeton Applied Research).

CORR electrolysis in an H-cell

The working electrode was arranged in a three-electrode configuration, with a SCE serving as the reference electrode (Hach), and a platinum foam (Goodfellow) serving as the counterelectrode. The counterelectrode was placed inside an anolyte compartment bridge, which contained the same electrolyte, and was separated from the catholyte by a glass frit. The applied potential conversion from SCE reference to RHE reference followed the equation: E (V versus RHE) = E (V versus SCE) + 0.244 + 0.059pH.

Prior to the electrolysis, the gas of interest (argon and CO both from Air Liquide) was flushed for 20 min. After 20 min, the gas flow was stopped, and the electrolysis experiment was then initiated. After electrolysis, 100 µl of gas headspace above the catholyte was sampled using a gas-tight syringe (Hamilton) inserted through the rubber septum and injected into a gas chromatography–thermal conductivity detector system (Agilent Technologies 7820A GC) for analysis. The liquid products were analysed using a Bruker AC 400 MHz NMR spectrometer. A total of 392 µl of the solution of interest, 48 µl of D_2O (Sigma-Aldrich, 99%D), and 40 µl of a 4 mM DMSO (Sigma-Aldrich, anhydrous 99.8%) solution were mixed in an NMR tube. A minimum of 128 scans was accumulated using the water presaturation method with a relaxation time of 25 s. Quantification was performed relative to the DMSO peak.

Preparation of the porous 3D nickel electrodes

The nickel electrode in Fig. 3a was fabricated based on the technique of indirect 3D printing first introduced by Hereijgers et al.[39,40]. The electrode moulds were designed in the CAD software Autodesk Inventor 2019 and 3D printed in Formlabs Castable Wax resin on a Formlabs

Form-2 stereolithographic 3D printer. The paste consists of nickel powder (61.7 wt%), epoxy resin (10 wt%) and an aqueous solution of 3 wt% carboxymethylcellulose sodium salt (24.3 wt%) and sodium chloride (4 wt%)[41,42] (Supplementary Note 1).

The porosity of the electrode can be determined from the mass of water absorbed by the electrode pores (equation (1)):

$$\varphi = \frac{V_p}{V_p + V_s} = \frac{\frac{m_{H2O}}{\rho_{H2O}}}{\frac{m_{H2O}}{\rho_{H2O}} + \frac{m_{Ni}}{\rho_{Ni}}} = \frac{\frac{1.14\,g}{0.997\,g\,cm^{-3}}}{\frac{1.14\,g}{0.997\,gcm^{-3}} + \frac{3.451\,g}{8.908\,g\,cm^{-3}}} = 0.7469 \quad (1)$$

where m_{H2O} is the mass of absorbed water, m_{Ni} is the weight of the nickel electrode, ρ_{H20} is the density of water, ρ_{Ni} is the density of nickel, V_p is the volume of the pore space (water) and V_s is the volume of the solid material (nickel).

Deposition of porphyrins on the 3D nickel electrode (Fe-TPP/Ni)

As shown in Supplementary Fig. 12, iron porphyrins were synthesized beginning with the condensation of pyrrole and benzaldehyde by an electrophilic substitution reaction to form TTP as reported in our previous works[41,42]. It was then metalated using $FeCl_2$ to form Fe-TPP.

The fabricated 3D nickel electrode was first cleaned with acetone using ultrasound for 30 min. It was then rinsed thoroughly with acetone and left in a 1 M HCl solution overnight to remove surface oxides. The electrode was then rinsed with fresh 1 M HCl, followed by another acetone rinse. Finally, nitrogen gas was blown over the electrode to ensure all inner and outer pores were clean and dry. The electrode was dried in a vacuum oven at 50 °C for another 2 h. To clean the electrode after the CO_2RR reaction, it was sonicated and rinsed several times with DCM until the solution was completely colourless, ensuring no Fe-TPP remained on the electrode. The same cleaning procedure was then repeated to ensure the electrode was clean for the next reaction.

A solution of Fe-TPP (130 mg) in DCM (4 ml) was drop-cast onto the preprepared 3D nickel electrode and dried in a vacuum oven for 2 h. A change in electrode colour from grey to purple indicates the nickel electrode has been fully covered with purple Fe-TPP, making it easy to distinguish any uncovered surface area. The Fe-TPP catalyst concentration was calculated as 2.7×10^{-5} mol cm^{-2} relative to the geometric electrode area (5.16 cm^2).

Fabrication of the carbon black control electrode (Fe-TPP/C)

To evaluate the Fe-TPP catalyst performance and product composition in the absence of nickel, a replica of the sintered nickel electrode was 3D printed (SLA Formlabs Form-2, clear resin) and subsequently coated with carbon black to yield a conductive surface. A solution of Fe-TPP (130 mg) in DCM (4 ml) and 5% Nafion was then drop-cast on the carbon black electrode (Supplementary Fig. 29). Unlike the sintered nickel electrode, contacts could not be spot welded to the electrode surface. Instead, nickel contacts were pressed on the electrode surface and then glued with epoxy resin.

Cell design for the porous 3D electrodes

The three-electrode set-up comprised a RHE reference electrode (Mini-Hydroflex, Gaskatel), a nickel foam counterelectrode, and one of the described 3D electrodes (Ni, TPP-Ni, Fe-TPP/C and Fe-TPP/Ni). Using a custom-designed cell reactor allows for CO_2 to be bubbled through the bottom of the reactor and through the porous electrode channels. The cell set-up is shown in Supplementary Figs. 20–24.

Electrochemical measurements for the 3D electrodes

For each electrochemical reaction, the solution was first saturated with either CO_2 or Ar. The gas flow rate was then set using a gas flow controller (Supplementary Fig. 24) and purged through the bottom of the custom cell. The electrochemical studies were carried out using a P4000 potentiostat (Princeton Applied Research) with a three-electrode set-up. Deposited iron porphyrin onto nickel (Fe-TPP/Ni) served as a working electrode in the cathode chamber, nickel foam (auxiliary) and a RHE (reference electrode). Chronoamperometry measurements were performed using determined RHE potentials.

CO_2 electrolysis gas product analysis for the 3D electrodes

To estimate the FE of the gaseous products from the CO_2RR, the outlet flow of the cathode compartment was periodically analysed using a gas chromatograph (InterScience PerkinElmer Clarus 680) with two thermal conductivity detectors and a flame ionization detector. The concentration of gas products (CO and H_2) was calculated from an average of four gas chromatograph injections. For ideal gases, the volume fraction from gas chromatography equals the mole fraction. The mole fraction of water vapour exiting the reactor, measured with a humidity sensor, was 78% ($xH_2O = 0.023$). The mole fraction of CO_2 exiting was then calculated, knowing that the sum of the mole fractions is equal to 1.

$$x_{CO_2,out} = 1 - (x_{CO} + x_{H_2O} + x_{H_2}) \quad (2)$$

After calculating the mole fractions of all gaseous products, the volumetric flow rate at the outlet of the reactor was measured with the mass flow meter and used to calculate the moles of each product.

$$n_{CO} = \dot{V}_{outlet} \times x_{CO} \quad (3)$$

$$n_{H_2} = \dot{V}_{outlet} \times x_{H_2} \quad (4)$$

$$FE_{CO} = \frac{n_{CO} \times n^e \times F}{I} \times 100\% \quad (5)$$

where n_{CO} is the number of moles of CO produced per second, n^{e^-} is the number of electrons involved in the CO_2RR (two electrons for CO), F (Faraday constant) is 96,485 C mol^{-1} and I is the applied current (in A). $\dot{V}_{outlet}$ refers to the measured volumetric flow rate of the gas mixture (CO and H_2) exiting the reactor.

CO_2 electrolysis liquid product analysis for the 3D electrodes

Following the CO_2RR, electrolyte samples were taken from the cathode compartment. ^{1}H NMR was recorded with a Bruker 400 MHz spectrometer and processed using MestreNova. NMR analysis was performed on a mixture of 400 µl of electrolyte sample, 50 µl of dimethyl sulfoxide (DMSO) solution as internal standard and 50 µl of D_2O. ^{1}H NMR chemical shifts (δ) are reported as ppm in D_2O.

The liquid products were also analysed by high-pressure liquid chromatography (HPLC; Agilent 1290 Infinity II) to determine the composition of the liquid products. An Aminex HPX-87H organic acid analysis column was used for the HPLC analysis. The product peaks in the HPLC chromatogram of the experimental sample are compared with the calibration peaks of the reference components to determine the type of the component (by comparing the retention time) and its concentration (by comparing the area). The retention time of the observed peak is around 39–40 min, which corresponds to ethanol's retention time according to the HPLC calibration data. The concentration of ethanol is calculated using the formula:

$$C = m \times A \quad (6)$$

where C is the concentration of the product in mM, A is the area of the product peak and m is the slope of the calibration curve for the component. The calibration curve for a component was generated by analysing various concentrations of the component used for HPLC, such as 0.1 mM, 0.5 mM, 1 mM, 5 mM, 10 mM, 25 mM and 50 mM, and then plotting the peak areas of the component on the x axis and concentrations on the y axis to obtain the slope of the calibration curve, m. In the above

example, the concentration of ethanol in the experimental sample can be calculated to be 55.52 mM, using an m value of 7.0807×10^{-4} units.

Protocol for quantitative analysis of pervaporate concentration by gas chromatography

To provide greater information regarding the evolution of C_{2+} products, the volatile effluents (methanol, ethanol, propanol) in the CO_2-off-gas were detected by a flame ionization detector. This allowed us to see increases and decreases of products over time separately from the NMR and HPLC characterizations. Our calibration protocol for a quantitative use of this technique is outlined in Supplementary Fig. 33.

DFT computational details

DFT computations were performed using the Vienna Ab initio Simulation Package[43], on Compute Canada clusters. In all computations, we used the projected augmented wave pseudopotentials and the generalized gradient approximation of Perdew–Burke–Ernzerhof to describe the exchange-correlation functionals[44]. A cut-off energy of 450 eV for the plane-wave basis sets and a $2 \times 2 \times 1$ Γ-centred Monkhorst–Pack mesh for the k-point sampling in the first Brillouin zone, with a first-order Methfessel–Paxton smearing parameter σ of 0.05 eV, ensured that the energy convergence criteria are better than 1 meV for a vacuum of 20 Å or greater. The self-consistent field convergence criterion is set to 10^{-4} eV for electronic iteration, and the ionic relaxation continued until the maximum force was less than 0.02 eV $Å^{-1}$ which was updated by the conjugate gradient approach. Dipole corrections and spin polarization are implemented. The DFT-D3 method with Becke–Jonson damping is performed for the van der Waals correction. The electrostatic charge density around each ion is calculated by the Bader charge analysis method[45]. VESTA software is used for the visualization[46]. Structure optimization, electron density and delocalization calculations follow the standard procedures described in the literature[47].

Data availability

The raw and processed data that support the findings of this study are publicly available in the 4TU.ResearchData database with the identifier https://doi.org/10.4121/9247f0c0-aa90-4407-a81f-afe5809fe2bb.

References

1. Costentin, C., Robert, M. & Savéant, J.-M. Molecular catalysis of electrochemical reactions. *Curr. Opin. Electrochem.* **2**, 26–31 (2017).
2. Rao, H., Schmidt, L. C., Bonin, J. & Robert, M. Visible-light-driven methane formation from CO_2 with a molecular iron catalyst. *Nature* **548**, 74–77 (2017).
3. Shen, J. et al. Electrocatalytic reduction of carbon dioxide to carbon monoxide and methane at an immobilized cobalt protoporphyrin. *Nat. Commun.* **6**, 8177 (2015).
4. Bhugun, I., Lexa, D. & Savéant, J. Catalysis of the electrochemical reduction of carbon dioxide by iron(0) porphyrins: synergystic effect of weak Brönsted acids. *J. Am. Chem. Soc.* **118**, 1769–1776 (1996).
5. Boutin, E. et al. Aqueous electrochemical reduction of carbon dioxide and carbon monoxide into methanol with cobalt phthalocyanine. *Angew. Chem. Int. Ed.* **58**, 16172–16176 (2019).
6. Wu, J. et al. A metal-free electrocatalyst for carbon dioxide reduction to multi-carbon hydrocarbons and oxygenates. *Nat. Commun.* **7**, 13869 (2016).
7. Song, Y. et al. High-selectivity electrochemical conversion of CO_2 to ethanol using a copper nanoparticle/N-doped graphene electrode. *ChemistrySelect* **1**, 6055–6061 (2016).
8. Ma, W. et al. Electrocatalytic reduction of CO_2 to ethylene and ethanol through hydrogen-assisted C–C coupling over fluorine-modified copper. *Nat. Catal.* **3**, 478–487 (2020).
9. Hoang, T. T. H., Ma, S., Gold, J. I., Kenis, P. J. A. & Gewirth, A. A. Nanoporous copper films by additive-controlled electrodeposition: CO_2 reduction catalysis. *ACS Catal.* **7**, 3313–3321 (2017).
10. Li, F. et al. Cooperative CO_2-to-ethanol conversion via enriched intermediates at molecule–metal catalyst interfaces. *Nat. Catal.* **3**, 75–82 (2020).
11. Jouny, M., Luc, W. & Jiao, F. General techno-economic analysis of CO_2 electrolysis systems. *Ind. Eng. Chem. Res.* **57**, 2165–2177 (2018).
12. Jiang, K. et al. Metal ion cycling of Cu foil for selective C–C coupling in electrochemical CO_2 reduction. *Nat. Catal.* **1**, 111–119 (2018).
13. Liang, Z.-Q. et al. Copper-on-nitride enhances the stable electrosynthesis of multi-carbon products from CO_2. *Nat. Commun.* **9**, 3828 (2018).
14. Ren, D., Ang, B. S.-H. & Yeo, B. S. Tuning the selectivity of carbon dioxide electroreduction toward ethanol on oxide-derived Cu_xZn catalysts. *ACS Catal.* **6**, 8239–8247 (2016).
15. Abdinejad, M. et al. Electrocatalytic reduction of CO_2 to CH_4 and CO in aqueous solution using pyridine–porphyrins immobilized onto carbon nanotubes. *ACS Sustain. Chem. Eng.* **8**, 9549–9557 (2020).
16. Wang, X. et al. Efficient electrically powered CO_2-to-ethanol via suppression of deoxygenation. *Nat. Energy* **5**, 478–486 (2020).
17. Abdinejad, M. et al. Electroreduction of carbon dioxide to acetate using heterogenized hydrophilic manganese porphyrins. *Chem. Eur. J.* **29**, e202203977 (2023).
18. Savéant, J.-M. Molecular catalysis of electrochemical reactions. mechanistic aspects. *Chem. Rev.* **108**, 2348–2378 (2008).
19. Jackson, M. N., Kaminsky, C. J., Oh, S., Melville, J. F. & Surendranath, Y. Graphite conjugation eliminates redox intermediates in molecular electrocatalysis. *J. Am. Chem. Soc.* **141**, 14160–14167 (2019).
20. Tilley, S. D. Metal-like molecules. *Nat. Catal.* **5**, 359–360 (2022).
21. Murphy, B. E. et al. Homolytic cleavage of molecular oxygen by manganese porphyrins supported on Ag(111). *ACS Nano* **8**, 5190–5198 (2014).
22. Duncan, D. A. et al. Immobilised molecular catalysts and the role of the supporting metal substrate. *Chem. Commun.* **51**, 9483–9486 (2015).
23. Petraki, F. et al. Impact of the 3*d* electronic states of cobalt and manganese phthalocyanines on the electronic structure at the interface to Ag(111). *J. Phys. Chem. C* **115**, 21334–21340 (2011).
24. Petraki, F. et al. Modification of the 3*d*-electronic configuration of manganese phthalocyanine at the interface to gold. *J. Phys. Chem. C* **116**, 5121–5127 (2012).
25. Petraki, F. et al. Interaction between cobalt phthalocyanine and gold studied by X-ray absorption and resonant photoemission spectroscopy. *J. Phys. Chem. Lett.* **1**, 3380–3384 (2010).
26. Uihlein, J. et al. Communication: influence of graphene interlayers on the interaction between cobalt phthalocyanine and Ni(111). *J. Chem. Phys.* **138**, 81101–81104 (2013).
27. Schmid, M., Kaftan, A., Steinrück, H.-P. & Gottfried, J. M. The electronic structure of cobalt(II) phthalocyanine adsorbed on Ag(111). *Surf. Sci.* **606**, 945–949 (2012).
28. Costentin, C., Robert, M. & Savéant, J.-M. Current Issues in molecular catalysis illustrated by iron porphyrins as catalysts of the CO_2-to-CO electrochemical conversion. *Acc. Chem. Res.* **48**, 2996–3006 (2015).
29. Hori, Y. in *Modern Aspects of Electrochemistry* (eds Vayenas, C. G. et al.) 89–189 (Springer, 2008); https://doi.org/10.1007/978-0-387-49489-0_3
30. Zhou, Y. et al. Long-chain hydrocarbons by CO_2 electroreduction using polarized nickel catalysts. *Nat. Catal.* **5**, 545–554 (2022).

31. Zeng, Z. et al. Orbital coupling of hetero-diatomic nickel–iron site for bifunctional electrocatalysis of CO_2 reduction and oxygen evolution. *Nat. Commun.* **12**, 4088 (2021).
32. Westre, T. E. et al. A multiplet analysis of Fe K-Edge 1s → 3*d* pre-edge features of iron complexes. *J. Am. Chem. Soc.* **119**, 6297–6314 (1997).
33. Römelt, C. et al. Electronic structure of a formal iron(0) porphyrin complex relevant to CO_2 reduction. *Inorg. Chem.* **56**, 4745–4750 (2017).
34. Kumar, A. Interfacial electronic properties of FeTPP-Cl on HOPG. *Mater. Today Proc.* **57**, 898–901 (2022).
35. Vos, R. E. & Koper, M. T. M. Nickel as electrocatalyst for CO_2 reduction: effect of temperature, potential, partial pressure, and electrolyte composition. *ACS Catal.* https://doi.org/10.1021/acscatal.4c00009 (2024).
36. Jouny, M., Luc, W. & Jiao, F. High-rate electroreduction of carbon monoxide to multi-carbon products. *Nat. Catal.* **1**, 748–755 (2018).
37. Li, N., Su, Z., Coppens, P. & Landrum, J. X-ray diffraction study of the electronic ground state of (meso-tetraphenylporphinato) iron(II). *J. Am. Chem. Soc.* **112**, 7294–7298 (1990).
38. Hunter, S. C. et al. Intermolecular interactions in solid-state metalloporphyrins and their impacts on crystal and molecular structures. *Inorg. Chem.* **53**, 11552–11562 (2014).
39. Hereijgers, J., Schalck, J., Lölsberg, J., Wessling, M. & Breugelmans, T. Indirect 3D printed electrode mixers. *ChemElectroChem* https://doi.org/10.1002/celc.201801436 (2019).
40. Hereijgers, J., Schalck, J. & Breugelmans, T. Mass transfer and hydrodynamic characterization of structured 3D electrodes for electrochemistry. *Chem. Eng. J.* **384**, 123283 (2019).
41. Abdinejad, M. et al. Enhanced electrochemical reduction of CO_2 catalyzed by cobalt and iron amino porphyrin complexes. *ACS Appl. Energy Mater.* **2**, 1330–1335 (2019).
42. Abdinejad, M., Dao, C., Zhang, X. & Kraatz, H. B. Enhanced electrocatalytic activity of iron amino porphyrins using a flow cell for reduction of CO_2 to CO. *J. Energy Chem.* **58**, 162–169 (2021).
43. Kresse, G. & Hafner, J. Ab initio molecular dynamics for liquid metals. *Phys. Rev. B* **47**, 558–561 (1993).
44. Perdew, J. P., Burke, K. & Ernzerhof, M. Generalized gradient approximation made simple. *Phys. Rev. Lett.* **77**, 3865–3868 (1996).
45. Henkelman, G., Arnaldsson, A. & Jónsson, H. A fast and robust algorithm for Bader decomposition of charge density. *Comput. Mater. Sci.* **36**, 354–360 (2006).
46. Momma, K. & Izumi, F. VESTA: a three-dimensional visualization system for electronic and structural analysis. *J. Appl. Crystallogr.* **41**, 653–658 (2008).
47. Al-Mahayni, H., Wang, X., Harvey, J.-P., Patience, G. S. & Seifitokaldani, A. Experimental methods in chemical engineering: density functional theory. *Can. J. Chem. Eng.* **99**, 1885–1911 (2021).

Acknowledgements

R.M.-G. and F.M. acknowledge NWO project 15169 for infrastructure support. A.S. acknowledges support received from an NSERC Discovery Grant (RGPIN-2020-04960) and the Canada Research Chair (950-23288). M.R. acknowledges the Institut Universitaire de France (IUF) for partial financial support. The DFT computations carried out in this study was supported by Calcul Quebec, Compute Canada. The XAS measurements were performed at the Canadian Light Source (CLS) under project 36G12729. T.B. thanks E. Pidko and M. Jackson for mechanistic discussions during the project, and D. Ripepi for the SEM study.

Author contributions

M.A. conceived the initial project. M.A. synthesized the molecular catalysts. R.M.-G. designed and built the flow cell and the 3D structured nickel and carbon electrodes. M.A. and R.M.-G. set up, performed and optimized cell design for the initial sets of flow experiments leading to ethanol formation. M.A. performed the parameterization and stability tests of the 3D porous electrode flow-cell experiments and the 3D electrode material characterizations. A.F. and A.S. performed the DFT computations, and analysed and discussed the results. A.F. also performed the XAS experiments. A.S. supervised the computations and the in situ XAS experiments. C.L. and J.S. performed the CO_2 and CO experiments of Fe-TPP drop-cast on nickel foam, which were supervised and checked by M.R. T.B. supervised the project. The work was written and edited by all coauthors.

Competing interests

The authors declare no competing interests.

Additional information

Supplementary information The online version contains supplementary material available at https://doi.org/10.1038/s41929-024-01225-1.

Correspondence and requests for materials should be addressed to Maryam Abdinejad, Ali Seifitokaldani or Thomas Burdyny.

Peer review information *Nature Catalysis* thanks Joshua Wright and the other, anonymous, reviewer(s) for their contribution to the peer review of this work.